

ATR and Reflectance IR Spectroscopy, Applications

UP Fringeli, University of Vienna, Austria

© 1999 Elsevier Ltd. All rights reserved.

This article is reproduced from the previous edition, volume 1, pp 58–75, © 1999, Elsevier Ltd.

Symbols

A	absorbance (decadic)
d	sample thickness
d_e	<i>effective thickness</i> (Harrick)
d_p	penetration depth
\bar{d}	mean penetrated layer thickness
E	electric field
E_x	electric field component in x-direction
E_y	electric field component in y-direction
E_z	electric field component in z-direction
J	energy flux (time average)
m_x	x-component of the unit vector in the direction of <i>M</i>
m_y	y-component of the unit vector in the direction of <i>M</i>
m_z	z-component of the unit vector in the direction of <i>M</i>
M	transition dipole moment
n	refractive index
\hat{n}	complex refractive index
N	number of active internal reflections
r	ratio of reflected to incident field
R^{ATR}	dichroic ratio related to ATR spectra
R	dichroic ratio
R	reflectance
S_y = S_{mol}	molecular order parameter
S_δ	tilt order parameter
S_θ	order parameter with respect to the molecular axis
S_{seg}	segmental order parameter
S	Poynting vector (time average)
t	ratio of transmitted to incident field
T	transmittance
z	distance from surface
 , ⊥	parallel- and perpendicular- polarized light, respectively
*	conjugate complex
α	absorption coefficient
α	angle between transition dipole moment and z-axis
δ	phase shift
ε	permittivity
ε	molar absorption coefficient
ε₀	permittivity of vacuum

ε_r	relative permittivity (dielectric constant)
η	amplitude
θ_c	critical angle
θ_i	angle of incidence
θ_r	angle of reflection
θ_t	angle of refraction (transmission)
κ	absorption index
λ	wavelength
μ	permeability
μ₀	permeability of vacuum
μ_r	relative permeability
ν	number of equal functional groups per molecule
$\tilde{\nu}$	wavenumber
ρ	reflectance
τ	transmittance
τ	relaxation time
Γ	surface concentration
φ	phase lag
ω	angular frequency

Introduction

Chemical reactions that occur at gas–solid and liquid–solid interfaces are of central importance to a variety of research and technological areas, including biomembranes, drug design, drug–membrane interaction, biosensors, chemical sensors, heterogeneous catalysis, thin film growth, semiconductor processing, corrosion and lubrication. Many methods are used for interface studies, ranging from most simple ones like the octanol–water two-phase system for mimicking the partition of a drug between a biomembrane and the surrounding water, to most specialized and expensive techniques such as low-energy electron diffraction (LEED), Auger electron spectroscopy (AES), X-ray photoelectron spectroscopy (XPS/ESCA) and ion scattering spectroscopy (ISS).

Among this palette of techniques, optical reflection spectroscopy in the mid- and near-IR range occupies an important complementary position. The basic equipment consists of a commercial IR spectrometer and a suitable reflection accessory that usually fits into the sample compartment of the spectrometer. Many reflection techniques permit *in situ* applications, and if applied in

¹In Memory of N Jim Harrick.

the mid-IR, result in quantitative and structural information on a molecular level. Moreover, IR reflection spectroscopy features a very high performance-to-price ratio.

There is a wide range of different spectroscopic reflection techniques. First one should distinguish between internal (total) and external reflections. Attenuated total reflection (ATR) belongs to the first group. It makes use of the evanescent wave existing at the interface of the IR waveguide and the sample. Commercial ATR attachments differ mainly in shape and mounting of the internal reflection element (IRE) in the light path. Most IREs enable multiple internal reflections, a prerequisite for monolayer and sub-monolayer spectroscopy, and referred to as MIRE.

A variety of external reflection techniques are in use. In specular reflection (SR), the radiation reflected from the front surface of a bulk sample is collected. SR is often measured at or near-normal incidence. Reflected spectral energy depends on the absorption behaviour of the sample. In regions of strong absorption, the reflected energy is enhanced with respect to nonabsorbing spectral regions; moreover, the reflection spectrum is usually very different from a corresponding absorption (AB) spectrum obtained by a transmission experiment. AB spectra may, however, be calculated from SR spectra by means of the Kramers–Kronig transformation (KKT). Corresponding software for SR data processing is supplied with most commercial IR instruments. While specular reflectance is measured at or near-normal incidence, IR reflection–absorption spectroscopy (IRRAS) works from approximately 10° to grazing incidence. In this case the sample is placed on a reflecting substrate, usually a metal. The portion of reflected light from the sample surface is generally small compared with the energy reflected off the metal surface. Therefore, IRRAS data and transmission (T) data are analogous. From Fresnel's equations (see later), it follows that parallel (\parallel) and perpendicular (\perp) polarized electromagnetic waves undergo different phase shifts upon reflection. This phase shift is 180° for \perp -polarized light at nonabsorbing interfaces. As a consequence, incoming and reflected beams cancel at the interface (node). However, at large angles of incidence \parallel -polarized incident light results in an enhanced electric field component perpendicular to the reflecting interface (z -axis). For thin samples, that is sample thickness (d) much smaller than the quarter wavelength ($\lambda/4$) of the reflected light, RA spectra report only partial information on orientation. It should be noted, however, that for a complete orientation analysis spectra obtained with light polarized in the plane of the interface (x, y -plane) is also necessary. ATR fulfils this requirement, in contrast to RA.

Diffuse reflectance (DR) is successfully applied to obtain IR spectra of rough (scattering) or dull surfaces, that is of media intractable by other reflection techniques.

The interpretation of DR spectra, however, is sometimes handicapped by the fact that they may be a mixture of AB and SR spectra. DR spectroscopy is a sensitive tool, especially when used with an IR Fourier transform (FT) spectrometer (DRIFT).

Elucidation of structure–activity relationships is the aim of many applications of reflection spectroscopy to thin layers at interfaces. In this context, polarization measurements are of considerable importance, since molecules at interfaces exhibit often induced ordering.

Low signal intensities are common in different kinds of interface spectroscopy, especially when the sample consists of a monolayer or even submonolayer as usual in heterogeneous catalysis and substrate–biomembrane interaction. Although modern FTIR spectrometers exhibit very high stability, signal-to-noise (S/N) ratio enhancement by data accumulation is limited by environmental and instrumental instabilities. The fact that most commercial FT instruments are operated in a single-beam (SB) mode is disadvantageous in this respect, because the longer an experiment lasts, the greater is the time lag between sample and reference data, which facilitates the intrusion of instabilities. Several optional extras are available to reduce the time lag between acquisition of sample and reference spectra.

One possibility is the conversion of the single-beam instrument into a pseudo-double-beam instrument by means of a shuttle which moves alternately the sample and reference into the IR beam. Such attachments were first developed for transmission experiments and were later adapted for ATR measurements. In the latter case, the sample and the reference are placed on top of one another on the same trapezoidal MIRE. A parallel beam of half the height of the MIRE is directed alternately through the upper and lower half of the MIRE by computer-controlled vertical displacement of the ATR cuvette. This method is referred to as single-beam sample reference (SBSR) technique and is described in more detail later.

Polarization modulation (PM) in combination with IRRAS is a further possibility to enhance instrumental stability and background compensation when working at grazing incidence to a thin sample on a metal substrate. PM at approximately 50 kHz is achieved by means of a photoelastic modulator (PEM). Since under these experimental conditions the sample will only absorb light in the \parallel -polarized half-wave, the \perp -polarized half-wave of the signal is representative of the background, that is of the reference. Subtraction is performed by the lock-in technique within each PM cycle, that is 50 000 times per second. As a consequence, environmental and instrumental contributions are largely compensated.

Finally, it should be noted that a more general application of modulation spectroscopy can be used to obtain selective information on an excitable sample.

Modulated excitation (ME) spectroscopy can always be applied with samples allowing periodic stimulation via a periodic variation of any external thermodynamic parameter, for example temperature, pressure, concentration, electric field, and light flux. ME causes a periodic variation of the absorbance at those wavelengths that are typical for the molecules involved in the stimulated process. Phase-sensitive detection (PSD) by the digital lock-in technique adapted for FTIR instruments permits spectral registration of the modulated, that is affected, part of the sample. A typical feature of ME with PSD is the comparison of sample and reference within each period of stimulation. Within this time interval environmental and instrumental parameters are usually stable so that a very good baseline is achieved. Moreover, if one or more relaxation times τ_i of the kinetic response of the stimulated sample fulfil the condition $0.1 < \omega\tau_i < 10$, where ω denotes the angular frequency of stimulation, significant phase lags ϕ_i between stimulation and sample responses will occur which are related to the reaction scheme and the rate constants of the stimulated process.

Theory of Reflectance Spectroscopy

For a comprehensive description of the theory of reflectance, the reader is referred to the Further Reading section. In this article, theory will only be presented when necessary for a general understanding.

Fresnel's Equations

The theory of reflection and transmission of an electromagnetic wave by a plane boundary was first derived by Fresnel. The geometry of SR and transmission is depicted in **Figure 1**. The incident (i) plane wave consists of the parallel (\parallel) and perpendicular polarized (\perp) electric field components $E_{i\parallel}$ and $E_{i\perp}$, respectively. The corresponding components of the reflected (r) and refracted (transmitted t) field components are denoted by $E_{r\parallel}$, $E_{r\perp}$, $E_{t\parallel}$ and $E_{t\perp}$. Fresnel's equations relate the reflected and transmitted components to the corresponding incident components.

For a non-absorbing medium, that is for the absorption indices κ_1 and κ_2 equal to zero, one obtains for the ratio r between reflected and incident electric field

$$\begin{aligned} r_{\parallel} &= \frac{E_{r\parallel}}{E_{i\parallel}} = \frac{n_2 \cos \theta_i - n_1 \cos \theta_t}{n_2 \cos \theta_i + n_1 \cos \theta_t} \\ r_{\perp} &= \frac{E_{r\perp}}{E_{i\perp}} = \frac{n_1 \cos \theta_i - n_2 \cos \theta_t}{n_1 \cos \theta_i + n_2 \cos \theta_t} \end{aligned} \quad [1]$$

where \parallel and \perp denote parallel and perpendicular polarization, according to **Figure 1**. Eqn [1] may be

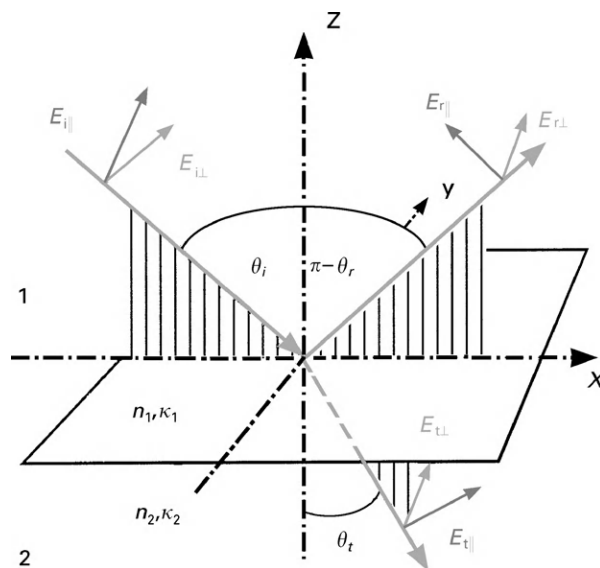


Figure 1 Specular reflection and transmission. The angles of incidence (i), reflection (r) and refraction (t) are denoted by θ_i , θ_r and θ_t , respectively. The corresponding electric field components are denoted by E . They are split into orthogonal portions, one parallel to the plane of incidence (x, z -plane) and the other perpendicular to this plane (parallel to y -axis). Accordingly, electric fields are referred to as parallel (\parallel) and perpendicular (\perp) polarized; n_1 , n_2 , κ_1 and κ_2 denote the refractive and absorption indices in the two media.

modified by introducing Snell's law of refraction:

$$n_1 \sin \theta_i = n_2 \sin \theta_t \quad [2]$$

resulting in

$$\begin{aligned} r_{\parallel} &= \frac{E_{r\parallel}}{E_{i\parallel}} = \frac{\tan(\theta_i - \theta_t)}{\tan(\theta_i + \theta_t)} \\ r_{\perp} &= \frac{E_{r\perp}}{E_{i\perp}} = -\frac{\sin(\theta_i - \theta_t)}{\sin(\theta_i + \theta_t)} \end{aligned} \quad [3]$$

As concluded from eqn [3], perpendicular polarized incident light undergoes a phase shift of 180° upon reflection, that there is a node at the reflecting interface resulting in zero electric field strength at this point. However, parallel polarized components remain in-phase. However, this conclusion holds no longer in the case of absorbing media.

The corresponding equations for the ratio t between transmitted and incident electric fields are

$$\begin{aligned} t_{\parallel} &= \frac{E_{t\parallel}}{E_{i\parallel}} = \frac{2n_1 \cos \theta_i}{n_2 \cos \theta_i + n_1 \cos \theta_t} \\ t_{\perp} &= \frac{E_{t\perp}}{E_{i\perp}} = \frac{2n_1 \cos \theta_i}{n_1 \cos \theta_i + n_2 \cos \theta_t} \end{aligned} \quad [4]$$

To modify eqns [1], [3] and [4] for absorbing media one has to introduce the complex refractive index. For an incoming plane-wave it is given by:

$$\hat{n} = n + i\kappa \quad [5]$$

where n is the refractive index and κ is the absorption index. As a consequence, r and t become complex and the resulting phase shifts differ from 0° and 180° as mentioned.

Energy Flux Density

The flux density of an electromagnetic wave is described by the Poynting vector. For the case of the plane-wave field, one obtains for the time average in the direction of propagation:

$$\bar{S} = \frac{1}{2} \sqrt{\varepsilon/\mu} E_0^2 \quad [6]$$

where μ is the permeability, that is the product of the permeability of vacuum μ_0 and the relative permeability μ_r which is unity for non-conductive materials, and ε denotes the permittivity which is the product of the permittivity of vacuum ε_0 and the relative permittivity (dielectric constant) ε_r which is complex for absorbing media, according to

$$\begin{aligned} \hat{\varepsilon}_r &= \hat{n}^2 = n^2 - \kappa^2 + i \cdot 2n\kappa \\ &= (n^2 + \kappa^2) \cdot \exp \left[i \cdot \operatorname{atan} \left(\frac{2n\kappa}{n^2 - \kappa^2} \right) \right] \\ &= |\hat{\varepsilon}_r| \cdot \exp(i \cdot \phi) \end{aligned} \quad [7]$$

Introducing the absolute value of eqn [7] into eqn [6] results in, for non-conducting media,

$$\bar{S} = \frac{1}{2} \sqrt{\varepsilon_0/\mu_0} \sqrt{n^2 + \kappa^2} E_0^2 \quad [8]$$

Reflectance ρ and transmittance τ are defined as the ratios of the corresponding energy fluxes \bar{J} . According to eqn [8] they are proportional to the square of the electric field, that is

$$\rho = \frac{\bar{J}_r}{\bar{J}_i} = rr^* \quad \text{and} \quad \tau = \frac{\bar{J}_t}{\bar{J}_i} = \frac{\sqrt{(n_2^2 + \kappa_2^2)} \cos \theta_t}{\sqrt{(n_1^2 + \kappa_1^2)} \cos \theta_i} tt^* \quad [9]$$

The factor $\sqrt{(n_2^2 + \kappa_2^2)}/\sqrt{(n_1^2 + \kappa_1^2)}$, which reduces to n_{21} for non-absorbing media, results from the change of dielectric (see eqn [8]), and $\cos \theta_t/\cos \theta_i$ takes account of the different cross-sections of the beam in media 1 and 2, respectively.

rr^* and tt^* , become r^2 and t^2 for non-absorbing media. In this case, eqns [1], [2] and [8] result in

$$\begin{aligned} \rho_{\parallel} &= \left(\frac{n_{21}^2 \cos \theta_i - \sqrt{n_{21}^2 - \sin^2 \theta_i}}{n_{21}^2 \cos \theta_i + \sqrt{n_{21}^2 - \sin^2 \theta_i}} \right)^2 \\ \rho_{\perp} &= \left(\frac{\cos \theta_i - \sqrt{n_{21}^2 - \sin^2 \theta_i}}{\cos \theta_i + \sqrt{n_{21}^2 - \sin^2 \theta_i}} \right)^2 \end{aligned} \quad [10]$$

where n_{21} denotes the ratio of refractive indices of media 2 and 1, respectively (see Figure 1). For normal incidence, that is $\theta_i=0$, eqn [10] reduces to

$$\rho_{\parallel} = \rho_{\perp} = \left(\frac{n_{21} - 1}{n_{21} + 1} \right)^2 \quad [11]$$

To obtain the reflectance of an absorbing medium one may introduce eqn [5] into eqn [10] or [11]. The result for normal incidence is

$$\rho_{\parallel} = \rho_{\perp} = \frac{(n_2 - n_1)^2 + (\kappa_2 - \kappa_1)^2}{(n_2 + n_1)^2 + (\kappa_2 + \kappa_1)^2} \quad [12]$$

It should be noted that in many applications medium 1 is air or a non-absorbing crystal, that is $\kappa_1=0$. It follows from eqn [12] that the reflectance increases with increasing absorption index of medium 2 (κ_2). In the limiting case of $\kappa_2 \rightarrow \infty$ one obtains $\rho \rightarrow 1$, that is a perfect mirror. Expressions for the more complicated case of oblique incidence to absorbing media have been derived (see Further Reading section).

The Kramers–Kronig Relations

For normal incidence ($\theta_i=0$) and non-absorbing medium 1 ($\kappa_1=0$, see Figure 1), one obtains from eqns [1] and [5] the following expression for the complex ratio $\hat{r}(\theta_i=0)$ between reflected and incident electric fields:

$$\begin{aligned} \hat{r}_{\parallel}(\theta_i=0) &= \frac{E_{r\parallel}}{E_{i\parallel}} = \frac{n_2 - n_1 + i\kappa_2}{n_2 - n_1 + i\kappa_2} = \eta \exp(i\phi) \\ \hat{r}_{\perp}(\theta_i=0) &= \frac{E_{r\perp}}{E_{i\perp}} = \frac{n_2 - n_1 + i\kappa_2}{n_2 - n_1 + i\kappa_2} = \eta \exp[i(\phi + \pi)] \end{aligned} \quad [13]$$

where η and ϕ are the amplitude and phase of $\hat{r}(\theta_i=0)$. They are functions of the wavenumber $\tilde{\nu}$ and related to each other by the Kramers–Kronig equations:

$$\begin{aligned} \ln \eta(\tilde{\nu}) &= \frac{2}{\pi} \int_0^{\infty} \frac{\nu \phi(\nu)}{\nu^2 - \tilde{\nu}^2} d\nu \\ \phi(\tilde{\nu}) &= \frac{2\tilde{\nu}}{\pi} \int_0^{\infty} \frac{\ln \eta(\nu)}{\nu^2 - \tilde{\nu}^2} d\nu \end{aligned} \quad [14]$$

Experimentally, $\eta(\tilde{\nu})$ can be determined, since it is related to the reflectance at normal incidence by

$\rho(\theta_i = 0) = \eta(\bar{\nu})\eta(\bar{\nu})^*$, that is $\eta(\bar{\nu}) = \sqrt{\rho(\theta_i = 0)}$; see eqn [12]. The Drude model may be used to extrapolate the measurement to $\bar{\nu} = 0$ and $\bar{\nu} = \infty$. From $\eta(\bar{\nu})$ and $\phi(\bar{\nu})$ the components of the refractive index can be calculated according to

$$\begin{aligned} n &= \frac{1 - \eta^2}{1 - 2\eta \cos \phi + \eta^2} \\ \kappa &= \frac{2\eta \sin \phi}{1 - 2\eta \cos \phi + \eta^2} \end{aligned} \quad [15]$$

For a detailed discussion, see the Further Reading section.

Internal Reflection Spectroscopy (ATR)

Internal reflection can only occur when the angle of the refracted beam θ_t is larger than the angle of incidence θ_i . This means, according to Snell's law (eqn [2]), that the refractive index of medium 2 must be smaller than that of medium 1 ($n_2 < n_1$). This is contrary to the situation in **Figure 1** where $n_2 > n_1$ was assumed. The region of total reflection begins when θ_t reaches 90° , that is at the critical angle of incidence θ_c . It follows from eqn [2] that

$$\sin \theta_c = \frac{n_2}{n_1} = n_{21} \quad [16]$$

It follows from eqns [2] and [16] for $\theta_i > \theta_c$ that $\sin \theta_t = \sin \theta_i / \sin \theta_c > 1$, resulting in a complex value for the corresponding cosine:

$$\cos \theta_t = \pm i n_{12} \sqrt{\sin^2 \theta_i - n_{21}^2} \quad [17]$$

The ratio r between internally reflected and incident electric field components is then obtained by introducing eqn [17] into eqn [1], resulting in

$$\begin{aligned} r_{\parallel} &= \frac{E_{r\parallel}}{E_{i\parallel}} = \frac{n_{21}^2 \cos \theta_i - i \sqrt{\sin^2 \theta_i - n_{21}^2}}{n_{21}^2 \cos \theta_i + i \sqrt{\sin^2 \theta_i - n_{21}^2}} \\ r_{\perp} &= \frac{E_{r\perp}}{E_{i\perp}} = \frac{\cos \theta_i - i \sqrt{\sin^2 \theta_i - n_{21}^2}}{\cos \theta_i - i \sqrt{\sin^2 \theta_i - n_{21}^2}} \end{aligned} \quad [18]$$

The corresponding equations for medium 2 are obtained by introducing eqn [17] into eqn [4], resulting in

$$\begin{aligned} t_{\parallel} &= \frac{E_{t\parallel}}{E_{i\parallel}} = \frac{2 \cos \theta_i}{n_{21} (\cos \theta_i - i \sqrt{\sin^2 \theta_i - n_{21}^2})} \\ t_{\perp} &= \frac{E_{t\perp}}{E_{i\perp}} = \frac{2 \cos \theta_i}{\cos \theta_i - i n_{21}^2 \sqrt{\sin^2 \theta_i - n_{21}^2}} \end{aligned} \quad [19]$$

Finally, it should be noted that incident electric fields undergo phase shifts in the ATR mode even if medium 2

is nonabsorbing. It follows from eqn [18] that

$$\begin{aligned} \tan \frac{\delta_{\parallel}}{2} &= \frac{\sqrt{\sin^2 \theta_i - n_{21}^2}}{n_{21}^2 \cos \theta_i} \\ \tan \frac{\delta_{\perp}}{2} &= \frac{\sqrt{\sin^2 \theta_i - n_{21}^2}}{\cos \theta_i} \end{aligned} \quad [20]$$

where δ_{\parallel} and δ_{\perp} are the phase shifts per internal reflection (no absorption) of \parallel -polarized and \perp -polarized incident light. Since the phase shifts and amplitudes are polarization dependent, linearly polarized incident light is elliptically polarized after an internal reflection. This phenomenon, however, does not hinder polarization measurement in the ATR mode.

Applications

Diffuse Reflectance

The geometry of a DR experiment is shown in **Figure 2**. The incident beam (I) is collimated to the sample S by means of the ellipsoidal mirror M_i . Two reflection mechanisms must be considered, specular reflection, R_s , and diffuse reflection, R_d . The former occurs at the surface and is governed by the Fresnel equations (eqns [1], [3] and [10–12]). As a consequence of anomalous dispersion, specular reflected light exhibits S-shaped intensity changes at the wavelengths of sample absorption. In contrast, diffuse reflected light exhibits absorption bands at frequencies observed also with transmitted light, but with intensities deviating significantly from those measured in a transmission experiment. The intensity of the DR spectrum may be described by the Bouguer–Lambert law (eqn [21]), the analogous expression to the Lambert–Beer law in transmission spectroscopy:

$$R_d = I_0 \exp(-\alpha \bar{d}) \quad [21]$$

where \bar{d} is the mean penetrated layer thickness, that is the depth of light penetration into the surface layer which

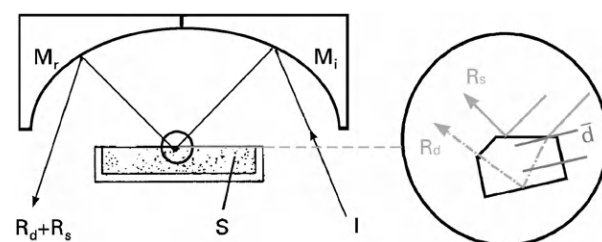


Figure 2 Diffuse reflection experiment. M_i, M_r = ellipsoidal mirrors for incident and reflected light; S = sample; I, R_d , R_s = incident diffuse, and specular reflected beams, respectively. In the magnified circle a possible ray tracing through a surface particle is shown, demonstrating the formation of mixed diffuse and specular reflected light. \bar{d} is the mean penetrated layer thickness according to the Bouguer–Lambert law (eqn [21]).

results in an intensity decrease by a factor of $1/e$, and α denotes the napierian absorption coefficient.

Diffuse reflectance infrared Fourier transform spectroscopy (DRIFT) has become a frequently used technique to obtain IR spectra from materials intractable by transmission spectroscopy. A number of high-performance reflection accessories are available from different manufacturers, allowing the detection of quantities down to the nanogram region. Nevertheless, DRIFT spectroscopy is confronted with two intrinsic problems: (1) the superposition of diffuse and specular reflected light (see [Figure 2](#)) which may lead to distorted line shapes and (2) the dependence of the mean penetration depth \bar{d} on the absorption coefficient. \bar{d} is found to be inversely proportional to the absorption coefficient α , thus leading to a certain levelling of the band intensities.

The disturbance by SR may be reduced considerably by technical means (trapping) on the reflection attachment. The resulting diffuse reflection spectrum then has to be corrected to correspond to the absorbance of a transmission spectrum. This mathematical procedure is generally performed according to the Kubelka–Munk theory. For a comprehensive and critical discussion of this theory the reader is referred to the Further Reading section.

Specular Reflection Spectroscopy

In specular reflectance, only light reflected off the front surface is collected (see [Figure 2](#)). The reflected energy is generally small ($<10\%$) for non-absorbing regions at normal or near-normal incidence. However, according to eqn [12], enhanced reflectance is observed in regions of sample absorption. As illustrated by [Figure 3](#), radiation intensity is different to transmission intensity, since S-shaped bands result as a consequence of anomalous dispersion of the refractive index in the region of an

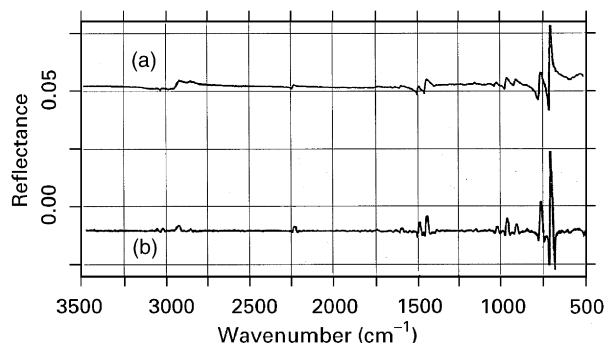


Figure 3 (a) Specular reflectance (SR) spectrum of a black acrylonitrile-butadiene-styrene polymer film measured at near-normal incidence, (b) Absorbance spectrum after data treatment of SR spectrum by a Kramers–Kronig transformation. Reproduced in part from [Zachman G \(1995\) *Journal of Molecular Structure* 348: 453–456](#), with permission of Elsevier Science.

absorption band. As a typical example, the specular reflectance spectrum of a black plastic is shown in [Figure 3](#).

Reflection Absorption Spectroscopy

Reflection Absorption Spectroscopy (RAS) at Near-normal Incidence

This is one of the most common and straightforward external reflection techniques. The IR beam is directed to the sample in the angular range $10\text{--}50^\circ$. The sample film must be on a reflective support. Under these conditions the RA spectrum is dominated by absorption since specular reflectance from the outer sample surface results in only 4–10% as shown in [Figure 4](#). For this reason RA spectra resemble transmission spectra very closely. Accordingly, typical sample thicknesses are between 0.5 and $20\ \mu\text{m}$.

RAS at Grazing Angle

Sensitivity at grazing angle is significantly enhanced with respect to near-normal reflectance and to transmission. The enhancement is explained by a polarization effect at the reflective surface. This effect is greatest for metal substrates and angles of incidence above 80° . As a general effect, \perp -polarized incident light has a node at the interface (see the preceding). The resulting reflectance will be very weak as long as the layer thickness is significantly smaller than $\lambda/4$. Therefore, \perp -polarized reflectance may be used as reference spectrum. \parallel -Polarized incident light produces electric field components in the x - and z -directions. On metal surfaces, however, the x - and y -components vanish, but the z -component is

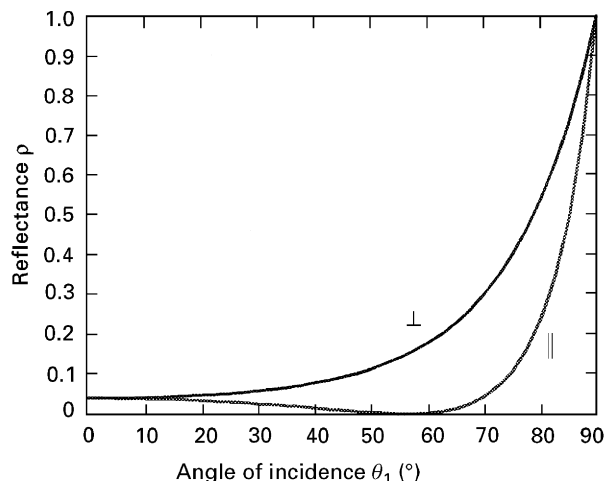


Figure 4 Specular reflectance calculated according to eqn [10]. Refractive indices: $n_1 = 1$ and $n_2 = 1.5$, \parallel , \perp denote parallel- and perpendicular-polarized incident light. The Brewster angle, where $\rho_{\parallel} = 0$ for a non-absorbing medium, is calculated as $\theta_1 = \theta_B = 56.3^\circ$, according to $\tan \theta_B = n_{21}$.

significantly enhanced owing to interference of incident and reflected beams. Compared with near-normal incidence, RAS magnification may be by more than one order of magnitude, thus permitting monolayer spectroscopy by a single reflection. Detailed information on RAS techniques applied to study carbon monoxide (CO) adsorbed on metal surfaces can be found in the Further Reading section.

More recently, RAS at grazing angle has been applied successfully for *in situ* spectroscopy of lipid monolayers and proteins at the air–water interface of a Langmuir trough, using the water surface as reflector (see Further Reading section).

Polarization Modulation RAS

This technique makes use of the fact that \perp -polarized incident light has a node at the reflecting interface resulting in zero absorbance at this point and nearly no absorbance of films significantly thinner than the quarter wavelength. Under these conditions, the \perp -reflectance spectrum may be used as a reference spectrum for the \parallel -reflectance spectrum. Since monolayer and submonolayer quantities of organic molecules result in low-intensity spectra, such measurements are susceptible to instrumental and environmental instabilities. This problem may be overcome by PM. For this purpose, a PEM is placed in the light path, leading to very fast periodic polarization changes of the incident light. The frequency range is 40–100 kHz, that is high enough to avoid interference's with the interferometer frequencies. Phase-sensitive demodulation of the PEM signal results in the interferogram of the difference between \parallel - and \perp -RA spectra, which is then normalized by division by the stationary response featuring the sum of \parallel - and \perp -mean reflectance according to

$$\frac{\Delta R}{R} = \frac{R_{\parallel} - R_{\perp}}{R_{\parallel} + R_{\perp}} \quad [22]$$

A description of an experimental set-up and of the relevant equations for PM-IRRAS can be found in the Further Reading section.

Instabilities are largely compensated because sample and reference spectra are measured and evaluated within one period, that is within 10–25 μ s. If applied in the IR region, this technique is referred to as PM-IRRAS.

It should be noted, however, that significant baseline problems may occur owing to different transmittance of \parallel - and \perp -polarized light by the spectrometer. This is demonstrated by the IRRAS data of a cadmium arachidate monolayer on a gold surface in Figure 5.

One should note that the usually intense absorption bands of CH_2 stretching, $\nu(\text{CH}_2)$ in the 2800–2950 cm^{-1} region and of CH_2 bending near 1470 cm^{-1} are very weak in the IRRAS spectrum in contrast to a corresponding dipalmitoylphosphatidic acid (DPPA) monolayer ATR

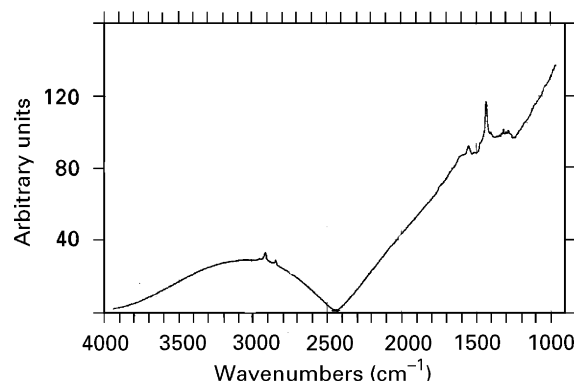


Figure 5 PM-IRRAS spectrum of an arachidic acid monolayer on a gold surface. The spectrum was normalized according to eqn [22]. It should be noted that only molecular vibration can be detected by IRRAS when the corresponding transition moment exhibits a component normal to the interface (z -direction). Reproduced in part with permission from Beccard B and Mapanowicz R (1995) *Nicolet Application Note AN-9542*. Madison, WI: Nicolet.

spectrum (see Figure 9). The reason is that IRRAS of thin layers on metallic surfaces offers only the electric field component normal to the interface, that is E_z , as already explained. The intensities of CH_2 stretching and CH_2 bending in Figure 5 are consistent with hydrocarbon chains of arachidic acid (ArAc) aligned along the normal to the interface. The lack of E_x and E_y components, that is of an electric field component parallel to the interface, disables the determination of a tilt angle. In this respect, IRRAS is at a disadvantage with respect to ATR, the technique presented in the following section. Moreover, ATR allows significantly better baseline control, especially if a special technique such as SBSR or ME is applied.

ATR Spectroscopy

A number of interesting conclusions may be drawn from eqns [18] and [19]. First, calculation of the reflectance according to eqn [9] results in $\rho_{\parallel} = \rho_{\perp} = 1$ which means *total reflection*. However, if medium 2 is absorbing, one has to insert the complex refractive index (eqn [5]) into eqn [18], resulting in $\rho_{\parallel} \neq \rho_{\perp} < 1$ which means *attenuated total reflection (ATR)*.

Second, to obtain more information on the nature of this process, one may calculate the propagation of a plane-wave in medium 2 under the conditions of total reflection. The result for a non-absorbing medium 2 is that there is no transmittance normal to the interface, that is $\tau_z = 0$; however, there is an energy flux in the x, y -plane near the interface, that is $\tau_x, \tau_y \neq 0$. Hence, there is an electromagnetic wave beyond the interface, although the whole energy is totally reflected. This wave is referred to as *evanescent wave*. Straightforward calculation results in that the electric field strength of this wave

decreases exponentially with distance z from the interface, according to

$$E_{x,y,z} = E_{0x,y,z} \exp\left[-\frac{z}{d_p}\right] \quad [23]$$

The subscripts x, y, z stand for the electric field components of the evanescent wave in the corresponding directions. Subscript 0 denotes the value at $z=0$ (interface in medium 2) and d_p is the so-called *penetration depth*, which results in

$$d_p = \frac{\lambda/n_1}{2\pi\sqrt{\sin^2\theta_i - n_{21}^2}} \quad [24]$$

where λ denotes the wavelength in vacuum and $\lambda/n_1 = \lambda_1$ is the wavelength in medium 1, that is, in the IRE. A typical ATR set-up is shown in **Figure 6**.

Hence, the penetration depth is the distance in the z -direction within which the electric field is decreased by a factor of $1/e$. This distance varies between a fraction of a micron and a few microns depending on the refractive indices of the IRE (e.g. $n_{Ge} = 4.0$, $n_{ZnSe} = 2.4$) and the medium 2 ($n_2 \approx 1.5$ for organic materials), as well as the angle of incidence. Harrick has given further practical details (see Further Reading section). As a consequence of Equations [23] and [24], the ATR spectrum features information on materials within a distance of one or a few d_p from the reflecting interface, resulting the highest sensitivity at the interface. Therefore, ATR spectroscopy is an optimum tool for *in situ* thin immobilized layer

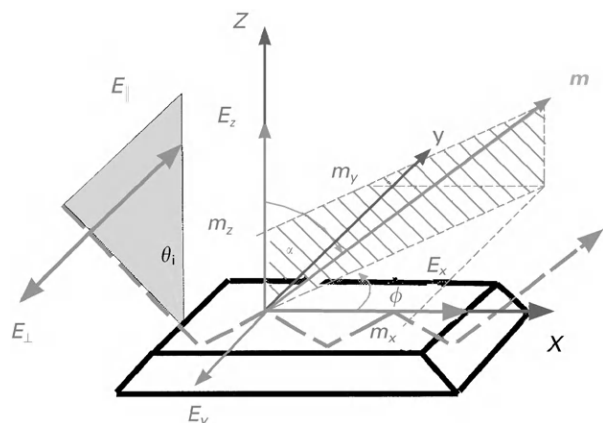


Figure 6 ATR set-up. Optical and structural features are related to the IRE fixed-coordinate system x, y, z . E_{\parallel} and E_{\perp} denote the parallel- and perpendicular-polarized electric field components of the light incident to the IRE under the angle θ_i . E_{\parallel} results in the E_x and E_z components of the evanescent wave, while E_{\perp} results in the E_y component. \mathbf{m} denotes the unit vector in the direction of the transition dipole moment vector of a given vibrational mode, and m_x, m_y, m_z are the corresponding components in the IRE coordinate system. \mathbf{m} goes off at an angle α with respect to the z -axis and the projection of \mathbf{m} to the xy -plane goes off at an angle ϕ with respect to the x -axis. Reproduced, from Fringeli UP, et al. (1998) *AIP Conference Proceedings* 430: 729–747, with permission of the American Institute of Physics.

analysis. For reviews on membrane spectroscopy the reader is referred to the Further Reading section.

Quantitative Analysis of ATR Spectra

The Concept of Effective Thickness

The concept of effective thickness was introduced by Harrick. The quantity d_e indicates the thickness of a sample that would result in the same absorbance in a hypothetical transmission experiment, as obtained with the genuine ATR experiment. This concept enables the straightforward application of the Lambert–Beer’s law on ATR data according to

$$T = 10^{-Ned_e} = 10^{-A} \quad [25]$$

where $A = Necd_e$ denotes the absorbance resulting from N internal reflections. For an isotropic layer extending from $z = z_i$ to $z = z_f$ one obtains

$$d_e^{iso} = \frac{1}{\cos\theta_i} \frac{n_2}{n_1} \frac{d_p}{2} E_{02}^2 \times \left[\exp\left(-\frac{2z_i}{d_p}\right) - \exp\left(-\frac{2z_f}{d_p}\right) \right] \quad [26]$$

According to eqn [26] d_e turns out to be wavelength dependent via d_p . As a consequence, ATR spectra of bulk media generally show increasing intensity with increasing wavelength. However, if the thickness of the layer $d = z_f - z_i$ is small compared with d_p then eqn [26] reduces to eqn [27] which is independent of the wavelength. E_{02}^r denotes the relative electric field component at the reflecting interface of medium 2. For $z_i = 0$ one obtains

$$d_e^{iso} = \frac{1}{\cos\theta_i} \frac{n_2}{n_1} d E_{02}^2 \quad [27]$$

For a bulk medium extending from $z_i = 0$ to $z_f = \infty$ eqn [26] results in

$$d_e^{iso} = \frac{1}{\cos\theta_i} \frac{n_2}{n_1} \frac{d_p}{2} E_{02}^2 \quad [28]$$

A more detailed presentation including an approximate calculation of the effective thickness for intermediate layer thickness, that is $d \approx d_p$, and references for a rigorous application of the general formalism are given in the Further Reading section.

Relative Electric Field Components

The relative electric field components E_{02}^r are obtained from eqns [19] according to

$$\begin{aligned} E_{02,\parallel}^r &= \sqrt{(t_{\parallel}^* t_{\parallel}^*)}; & E_{02,\perp}^r &= \sqrt{(t_{\perp}^* t_{\perp}^*)} \\ E_{02,x}^r &= E_{02,\parallel}^r \cdot \cos\theta_i; & E_{02,z}^r &= E_{02,\parallel}^r \cdot \sin\theta_i \\ E_{02,y}^r &= E_{02,\perp}^r \end{aligned} \quad [29]$$

Explicit expressions of eqns [29] for thin films and bulk media can be found in references in the Further Reading section.

Validity of the Effective Thickness Concept

Since the effective thickness concept permits the application of Lambert–Beer’s law to ATR data, experimental validation may be performed easily by comparing spectra of the same sample measured by both, ATR and transmission (T). As long as the results do not differ significantly from each other the formalism described earlier is considered to be applicable. ATR and T measurements with aqueous solutions of Na₂SO₄ have shown that at a 1 M concentration Lambert–Beer’s law is still fulfilled for the very intense SO₄²⁻ stretching band at 1100 cm⁻¹. Even for the strong H₂O bending [$\delta(\text{H}_2\text{O})$] band of liquid water at 1640 cm⁻¹ the integral molar absorption coefficients determined by ATR with a germanium IRE at an angle of incidence of $\theta_i = 45^\circ$ was found to be equal to T data within the experimental error. However, a few per cent deviations were found when peak values of the absorbance were used to determine the molar absorption coefficient. The latter indicates the onset of band distortion, a phenomenon well known in ATR spectroscopy under conditions of strong absorption. This finding is in accordance with calculations by Harrick using Fresnel’s equations with complex refractive indices. For Ge in contact with liquid water and $\theta_i = 45^\circ$ the analysis resulted in an upper limit of the absorption coefficient $\alpha_{\max} \approx 1000 \text{ cm}^{-1}$. The concept of effective thickness as described earlier may be considered to be valid for $\alpha < \alpha_{\max}$. For organic compounds this condition is generally fulfilled. In the case of $\delta(\text{H}_2\text{O})$ of liquid water, however, the absorption coefficient results in $\alpha = \varepsilon(1640 \text{ cm}^{-1})c = 1.82 \times 10^4 \text{ cm}^2 \text{ mol}^{-1} \times 5.56 \times 10^{-2} \text{ mol cm}^{-3} = 1011.9 \text{ cm}^{-1}$, which indicates that the limit of validity of the approach is reached, in complete accordance with experimental data mentioned earlier. Furthermore, it turned out that the anomalous dispersion in the range of strong water absorption bands should be taken into account if sample absorption within this range is analysed quantitatively.

Quantitative Analysis Taking Sample Absorption and Thickness into Account

The validity of Harrick’s weak absorber approximations has been checked by comparison with the general thickness- and absorption-dependent model. It was found that the formalism depicted in the preceding section may be used for film thicknesses up to 20 nm. Especially if the film is in contact with a third bulk medium, for example water, the deviation between accurate and approximate calculation of relative electric field components according to eqn [29] was found to be below 3%, that is within the error of most experiments. A comprehensive description of ATR spectroscopy of polymers using the general formalism can be found in the Further Reading section.

Since quantitative analysis of ATR data by the general formalism is very cumbersome, the use of more tractable approximations is recommended if possible. One possibility is the weak absorber approximations described in the preceding text; another approach was derived for the study of electrochemical reactions by ATR spectroscopy.

For more general information on quantitative methods and applications of ATR spectroscopy, see the Further Reading section.

Orientation Measurements

Considering a transition dipole moment M associated with a vibrational mode of a given molecule and the electric field E , responsible for vibrational excitation, the magnitude of light absorption depends on the mutual orientation of these two vectors according to eqn [30], which is the basis for orientation measurements. M_x , M_y and M_z denote the components of the transition dipole moment in the IRE fixed coordinate system shown in Figure 6.

$$\begin{aligned} A &= (E \cdot M)^2 \\ &= |E|^2 \cdot |M|^2 \cdot \cos^2(E, M) \\ &= (E_x M_x + E_y M_y + E_z M_z)^2 \end{aligned} \quad [30]$$

It is usual to work with dimensionless relative intensities instead of absolute intensities to get rid of physical and molecular constants, for example the magnitude of the transition moment. Introducing the so-called dichroic ratio R , the absorbance ratio obtained from spectra measured with \parallel - and \perp - polarized incident light, that is

$$\begin{aligned} R &= \frac{A_{\parallel}}{A_{\perp}} = \frac{d_{e,\parallel}}{d_{e,\perp}} \\ &= \frac{E_x^2 \langle m_x^2 \rangle + E_z^2 \langle m_z^2 \rangle + 2E_x E_z \langle m_x m_z \rangle}{E_y^2 \langle m_y^2 \rangle} \end{aligned} \quad [31]$$

where A and d_e denote absorbance and effective thickness relative to \parallel - and \perp - polarized incident light, respectively. E_x , E_y and E_z denote the relative electric field components according eqn [29]. $\langle m_x^2 \rangle$, $\langle m_y^2 \rangle$, $\langle m_z^2 \rangle$ and $\langle m_x m_z \rangle$ are ensemble mean values of the components of the unit vector in the direction of the transition dipole moment, see Figure 6. $\langle m_x m_z \rangle = 0$ for uniaxial orientation, for example isotropic distribution around all relevant orientation axes. On substitution of the unit vector components according to the geometry depicted in Figure 6, one obtains for the dichroic ratio

$$R^{\text{ATR}} = \frac{E_x^2}{E_y^2} + 2 \frac{E_z^2}{E_y^2} \frac{\langle \cos^2 \alpha \rangle}{1 - \langle \cos^2 \alpha \rangle} \quad [32]$$

where $\langle \cos^2 \alpha \rangle$ denotes the mean square cosine of the angle between the transition moment and the normal to

the interface. This quantity is accessible via two measurements, one with \parallel -polarization and the other with \perp -polarized incident light, resulting in R . The relative electric field components are available from Fresnel's eqns [19] with eqn [29]. For an isotropic sample, $\langle \cos^2\alpha \rangle_{\text{iso}} = 1/3$. Insertion of this value into eqn [32] results in

$$R_{\text{iso}}^{\text{ATR}} = \frac{E_x^2 + E_z^2}{E_y^2} \quad [33]$$

It should be mentioned that an isotropic sample results in $R=1$ in transmission but, according to eqn [33], not in ATR, where $R_{\text{iso}}^{\text{ATR}} \neq 1$. As an example, for total reflection with a bulk material 2 and $\theta_i=45^\circ$, one obtains $R_{\text{iso}}^{\text{ATR}} = 2.0$ irrespective of n_1 and n_2 , except $n_1 > n_2$.

The segmental order parameter S_{seg} is frequently used to characterize molecular ordering, for example to describe the fluctuation of a functional group in a molecule via the polarized absorption bands of a typical group vibration. For uniaxial orientation the order parameter is defined according to

$$S_{\text{seg}} = \frac{3}{2} \langle \cos^2\alpha \rangle - \frac{1}{2} \quad [34]$$

Thus, if the ATR geometry and the optical constants of the system are known, then S_{seg} may be determined measuring the dichroic ratio R of a given absorption band, followed by the calculation of the mean square cosine $\langle \cos^2\alpha \rangle$ and inserting this value into eqn [34]. A typical example is discussed later.

For more details and examples of application the reader is referred to the Further Reading section.

Determination of Surface Concentration

The effective thickness as indicated by eqns [26]–[28] holds for isotropic samples. Modification for oriented samples results

$$\begin{aligned} d_{\text{ex}} &= 3 \langle m_x^2 \rangle d_{\text{ex}}^{\text{iso}} = \frac{3}{2} (1 - \langle \cos^2\alpha \rangle) d_{\text{ex}}^{\text{iso}} \\ d_{\text{ey}} &= 3 \langle m_y^2 \rangle d_{\text{ey}}^{\text{iso}} = \frac{3}{2} (1 - \langle \cos^2\alpha \rangle) d_{\text{ey}}^{\text{iso}} \\ d_{\text{ez}} &= 3 \langle m_z^2 \rangle d_{\text{ez}}^{\text{iso}} = 3 \langle \cos^2\alpha \rangle d_{\text{ez}}^{\text{iso}} \end{aligned} \quad [35]$$

From eqn [25] and the relation $d_{e\parallel} = d_{\text{ex}} + d_{\text{ez}}$ and $d_{e\perp} = d_{\text{ey}}$, one obtains for the surface concentration Γ .

$$\begin{aligned} \Gamma &= c \cdot d = \frac{d \cdot A_{\parallel}}{v \cdot N \cdot d_{e\parallel} \cdot \varepsilon} = \frac{d \cdot \int A_{\parallel} d\tilde{\nu}}{v \cdot N \cdot d_{e\parallel} \cdot \int \varepsilon d\tilde{\nu}} \\ &= \frac{d \cdot A_{\perp}}{v \cdot N \cdot d_{e\perp} \cdot \varepsilon} = \frac{d \cdot \int A_{\perp} d\tilde{\nu}}{v \cdot N \cdot d_{e\perp} \cdot \int \varepsilon d\tilde{\nu}} \end{aligned} \quad [36]$$

where A_{\parallel} and A_{\perp} denote the absorbance measured with parallel- and perpendicular- polarized incident light,

respectively, ε is the molar absorption coefficient, ν denotes the number of equal functional groups per molecule and N is the number of active internal reflections. It should be noted that eqn [36] holds for peak absorbance and integrated absorbance, provided that the corresponding molar absorption coefficients are used.

Special Experimental ATR Techniques

SBSR Technique

Most FTIR spectrometers are working in the SB mode. As a consequence a single-channel reference spectrum has to be stored for later conversion of single-channel sample spectra into transmittance and absorbance spectra. This technique suffers inaccuracy owing to drifts resulting from the instrument, the sample or atmospheric absorption. To eliminate these unwanted effects to a great extent, a ATR attachment has been constructed, converting a single-beam instrument into a pseudo-double-beam instrument. The principle features of this attachment are depicted in **Figure 7**. As usual, a convergent IR beam enters the sample compartment. However, the focal point is now displaced from the centre of the sample compartment by means of the planar mirrors M1 and M2 to the new position F. The off-axis parabolic mirror M3 performs a conversion of the divergent beam into a parallel beam with fourfold reduced cross-section. This beam is focused to the entrance face of a trapezoidal MIRE by a cylindrical mirror M4. Therefore, the ray propagation in the MIRE is still parallel to the direction of light propagation (x -axis), enabling subdivision of the two reflective faces (x, y -planes) of the MIRE alongside at half-height. One half of the MIRE is then used for the sample (S) and the other one for the reference (R). Both S and R were encapsulated by flow-through cuvettes, independently accessible by liquids or gases. This principle is referred to as the SBSR technique.

SBSR absorbance spectra are calculated from sample and reference single-channel spectra which have been measured with a very short mutual time delay. A most favourable benefit of SBSR technique is that no wasted time for purging is required before starting a measurement after closing the sample compartment. Moreover, the whole sequence of single-channel spectra in the S and R channels is also available, allowing reconstruction of the history of each channel at any time by conventional data handling.

Modulated Excitation ME Spectroscopy and 2D IR Spectroscopy

Change of any external thermodynamic parameter generally exerts a specific influence on the state of a chemical system. The system response will be relaxation from the initial state (e.g. an equilibrium) to the final state (a new equilibrium state or a stationary state). In the case of a

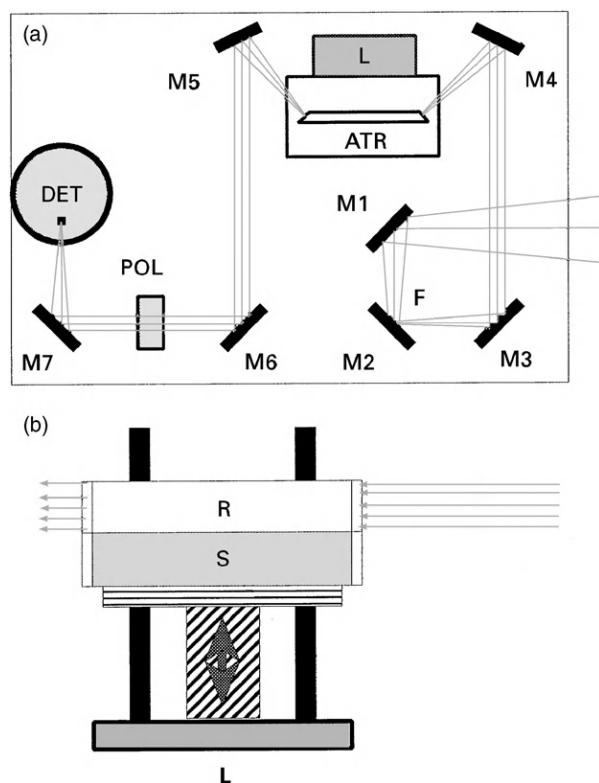


Figure 7 Single-beam sample reference (SBSR) ATR attachment. (a) The focus in the sample compartment is displaced to the position F by the planar mirrors M1 and M2. The off-axis parabolic mirror M3 produces a parallel beam with a diameter of 1 cm, that is half of the height of the MIRE. The cylindrical mirror M4 focuses the light to the entrance face of the MIRE. M5, which has the same shape as M4, reconverts to parallel light directing it via the planar mirror M6 through the polarizer POL, and it is then being focused to the detector DET by the off-axis parabolic mirror M7. (b) Alternating change from sample to reference is performed by computer-controlled lifting and lowering of the ATR cell body. Reproduced, from Fringeli UP et al. (1998) *AIP Conference Proceedings* 430: 729–747, with permission of the American Institute of Physics.

periodic change (modulation) of the parameter, the system response will also be periodic with angular frequency ω , relaxing from the initial state to a stationary state. All absorption bands of the spectrum which result from stimulated molecules or parts of them will be labelled by the frequency ω . As a consequence, it is possible to separate the modulated response of a system from the stationary response, resulting from parts of the system that were not affected by ME as well as from the background. More-over, if the kinetics of the stimulated process is in the same time range as the period of external excitation, phase lags and damped amplitudes will result. Both depend characteristically on the stimulation frequency, and therefore one can derive relevant information on the reaction scheme and the kinetics of the stimulated process (see also caption to [Figure 8](#)).

A variety of ME experiments have been reported. (1) Temperature ME of poly-L-lysine was used to study induced periodic secondary structural changes as well as the sequence of transients. (2) The classical ATR set-up (see [Figure 6](#)) facilitates the application of electric fields to immobilized thin films, such as biomembrane assemblies or to bulk materials such as liquid crystals, since a Ge ATR plate, supporting the membrane, may be used as one electrode, and the back-wall of the cuvette as counter electrode. (3) Hydration modulation was used to detect hydration sites of model membranes, (4) ME by UV radiation permitted kinetic studies of photoinduced chemical reactions and (5) ME by chemical substrates is a further versatile method to study chemically induced conformational changes of a sample immobilized to the MIRE. For that purpose, two computer-controlled pumps are used for periodic exchange of the liquid (water) environment of the sample in a flow-through cell. An example demonstrating the sensitivity and high quality of background compensation of ME techniques is presented later. The principles of ME spectroscopy are depicted schematically in [Figure 8](#).

2D FTIR Spectroscopy

Absorption bands in a set of modulation spectra that exhibit equal phase shifts with respect to the external stimulation are considered to be correlated. 2D correlation analysis is a statistical graphical means to visualize such a correlation in a 2D plot. Consequently, phase-resolved modulation spectra are data of a higher level and unambiguously allow a more direct and accurate evaluation. 2D plots look attractive, but one should be aware that the information content is lower than that of the underlying modulation spectra, first because band overlapping may result in inadequate phase information, and second because 2D spectra are affected much more by baseline errors than the original modulation spectra. A comprehensive discussion can be found in the Further Reading section.

Sensitivity of ATR Spectroscopy

Sensitivity of Stationary ATR Measurements

Commercial multiple internal reflection elements (MIRE) permit up to 50 internal reflections. This is generally enough for thin-layer spectroscopy in the nanometre or even subnanometre region. As an example, [Figure 9](#) shows a DPPA monolayer, that is a lipid monolayer of approximately 2 nm thickness, which has been transferred from approximately the air–water interface to a germanium MIRE by means of the Langmuir–Blodgett technique.

The dominant bands in [Figure 9](#) result from the stretching vibrations of 28 CH_2 groups of the two saturated hydrocarbon chains of the DPPA molecule. Looking at three resolved weaker bands gives an impression of the

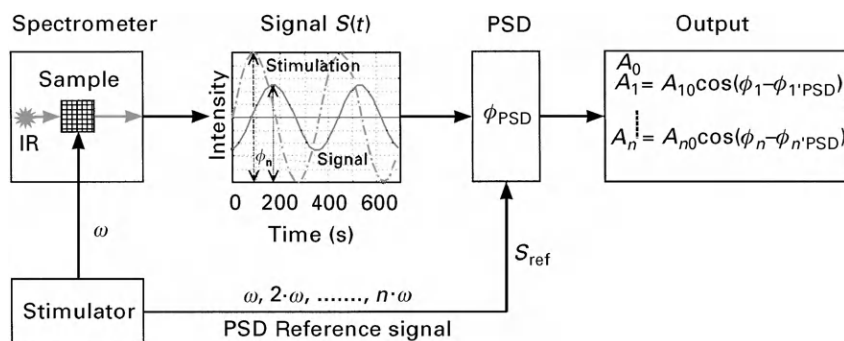


Figure 8 Schematic set-up for modulated excitation (ME) experiments. A periodic excitation is exerted on the sample with frequency ω . The sample response $S(t)$, as sensed by IR radiation, contains the frequency ω and higher harmonics at wavelengths that are significant for those parts of the sample that have been affected by the stimulation. Selective detection of the periodic sample responses is performed by phase-sensitive detection (PSD), resulting in the DC output and A_n of fundamental ω ($n=1$) and their harmonics $n\omega$ ($n=2, 3, \dots$), as well as the phase shifts ϕ_n between the n th harmonic and the stimulation. This phase shift is indicative of the kinetics of the stimulated process and of the underlying chemical reaction scheme. Since the PSD output A_n ($n=1, 2, \dots, n$; frequency $n\omega$) is proportional to $\cos(\phi_n - \phi_{n,PSD})$, absorption bands featuring the same phase shift ϕ_n are considered to be correlated, i.e. to be representative of a population consisting of distinct molecules or molecular parts. $\phi_{n,PSD}$ is the operator-controlled PSD phase setting. Because of the cosine dependence, different populations will have their absorbance maxima at different $\phi_{n,PSD}$ settings, thus allowing selective detection. Moreover, since in the case that $0.1 < \omega\tau_i < 10$ (τ_i denotes the i th relaxation time of the system), ϕ_n becomes ω dependent, $\phi_n = \phi_n(\omega)$. The spectral information can then be spread in the $\phi_{n,PSD} - \omega$ plane, resulting in a significant enhancement of resolution with respect to standard difference spectroscopy and time-resolved spectroscopy.

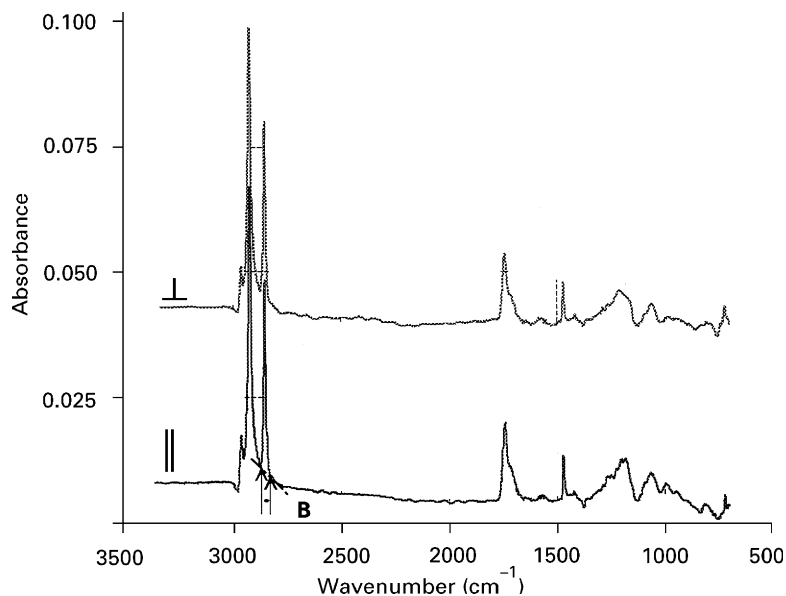


Figure 9 Parallel (||) and perpendicular (\perp) polarized ATR absorbance spectra of a dipalmitoylphosphatidic acid (DPPA) monolayer transferred at 30 mN m^{-1} from the aqueous subphase (10^{-4} M CaCl_2) to a germanium multiple internal reflection element (MIRE). Spectra were obtained from the dry monolayer in contact with dry air. A surface concentration of $\Gamma = 3.93 \times 10^{-10} \text{ mol cm}^{-2}$ was calculated by means of eqn [36] using the dichroic ratio of the symmetric CH_2 stretching vibration at 2850 cm^{-1} with respect to a linear baseline (B), resulting in $R^{\text{ATR}}[\nu^s(\text{CH}_2)] = 0.923$. Angle of incidence $\theta_i = 45^\circ$; number of equal functional groups $\nu = 28$; number of active internal reflections $N = 39$.

absorbance to be expected from a monomolecular coverage by functional groups of medium or weak molar absorption. The first is the terminal methyl group of the hydrocarbon chains. The antisymmetric stretching vibration, $\nu_{\text{as}}(\text{CH}_3)$, absorbs at $\sim 2960 \text{ cm}^{-1}$. As concluded from Figure 9, this monolayer results in a peak absorbance

of approximately 6 mAU. A weaker band is observed near 1420 cm^{-1} and may be assigned to the bending vibration of the α -methylene groups of the hydrocarbon chains, $\delta(\alpha\text{-CH}_2)$. Thus, an approximate monolayer of $\alpha\text{-CH}_2$ groups results in an absorbance of only about 1 mAU. Third, a monolayer of phosphate head groups results in more

intense absorption bands because of the larger transition dipole moment of the polar group. The corresponding absorbances of PO₃ stretching vibrations in the range 1000–1250 cm⁻¹ are between 5 and 10 mAU. It is concluded that conventional ATR measurements may allow significant access to bands of approximately 0.2–0.5 mAU, which correspond to 20–50% of a monolayer of weak absorbers.

Quantitative Analysis of Stationary ATR Spectra

The DPPA monolayer spectra shown in Figure 9 are now used to demonstrate the ease of application of the formalism for quantitative analysis of ATR spectra presented earlier.

Dichroic Ratio of Symmetric CH₂ Stretching

The dichroic ratio according to eqn [32] was calculated from the integrated absorbances of the symmetric CH₂ stretching bands, ν_s(CH₂), using linear baselines as marked in Figure 9 with lower and upper limits at 2828 and 2871 cm⁻¹, respectively. The corresponding integrals were found to be ∫ A_{||} dν̄ = 0.381 cm⁻¹, and ∫ A_⊥ dν̄ = 0.413 cm⁻¹, resulting in R^{ATR} = 0.923. This is the relevant experimental quantity.

Mean Orientation of Hydrocarbon Chains

Uniaxial orientation, that is isotropic distribution of DPPA around the z-axis, is assumed. The mean square cosine of the angle between the transition dipole moments of ν_s(CH₂) of the whole population of CH₂ groups of the molecule (28 groups in hydrocarbon chains, 1 in the glycerol part, slightly shifted in frequency) can be calculated from eqn [32], resulting in eqn [37].

$$\langle \cos^2 \alpha \rangle = \frac{(R^{\text{ATR}} - E_x^2/E_y^2)(E_y^2/E_z^2)}{2 + (R^{\text{ATR}} - E_x^2/E_y^2)(E_y^2/E_z^2)} \quad [37]$$

The squares of relative electric field components at the interface (z = 0) in medium 2 as calculated from eqn [29] for θ_i = 45°, n₁ = 4.0 (germanium), n₂ = 1.5 (DPPA monolayer) and n₃ = 1.0 (dry air) result in E_{ox,2}² = 1.991, E_{oy,2}² = 2.133 and E_{oz,2}² = 0.450. It follows that E_{o||,2}² = E_{ox,2}² + E_{oz,2}² = 2.441 and E_{o⊥,2}² = E_{oy,2}² = 2.133. The dichroic ratio for an isotropic film under these conditions would result in, according to eqn [33], R_{iso}^{ATR} = 1.144. Explicit equations for relative electric components calculated by means of Harrick's weak absorber approximation can be found in the Further Reading section.

Introducing the experimental value of R^{ATR} and the calculated squares of relative electric field components into eqn [37], one obtains for the mean square cosine of the angle between the transition moment of ν_s(CH₂) and the z-axis ⟨cos²α⟩ = -0.025. This value should not be negative because its minimum is zero; however, since it is

small, it is considered to be within experimental and predominately systematic errors. Therefore, is set ⟨cos²α⟩ = 0, resulting in α = 90°. This result requires that all methylene groups of the hydrocarbon chains assume an all-*trans* conformation and, moreover, all hydrocarbon chains are aligned normal to the MIRE, that is parallel to the z-axis (tilt angle 0°). The exact wave-number of the symmetric stretching vibration of the CH₂ group in glycerol is not known. However, overlapping with ν_s(CH₂) of the hydrocarbon chains is probable. Consequently, the bisector of the glycerol CH₂ group may also be concluded to be predominately parallel to the x, y-plane.

Mean Order Parameter of CH₂ Groups

The mean segmental order parameter resulting from eqn [34] is found to be $\bar{S}_{\text{seg}}[\nu_s(\text{CH}_2)] = -\frac{1}{2}$. This value is representative of a perfectly ordered molecular entity with isotropic arrangement of transition dipole moments around the z-axis and perfect parallel alignment to the interface (x,y-plane). It should be noted that for ⟨cos²α⟩ = 1, that is transition moments perfectly aligned normal to the interface (z-axis), eqn [34] results in the upper limit $\bar{S}_{\text{seg}} = 1$. Lipids in natural biomembranes consist of a considerable amount of unsaturated hydrocarbon chains. Since double bonds cause unavoidably *gauche* defects in elongated hydrocarbon chains, which leads to a reduced chain ordering, $\bar{S}_{\text{seg}}[\nu_s(\text{CH}_2)]$ is increased, reaching zero for an isotropic chain arrangement, since ⟨cos²α⟩ = 1/3 in this case.

It should be noted that the determination of order parameters of individual methylene groups in the hydrocarbon chains requires generally selective deuteration. In this respect, comprehensive deuterium NMR work should be mentioned (see Further Reading section).

A more general case of sample geometry is that of a transition moment being inclined by an angle Θ with respect to the molecular axis *a* and isotropically distributed around *a*. Furthermore, the molecular axis *a* forms an angle γ with respect to the tilt axis *t*, and is isotropically distributed around it, and finally, the axis *t* forming a tilt angle δ with the z-axis and is isotropically distributed around it. In this case, the segmental order parameter, for example S_{seg}[ν_s(CH₂)], may be expressed as superposition of three uniaxial orientations according to

$$\begin{aligned} S_{\text{seg}} &= \left(\frac{3}{2} \langle \cos^2 \delta \rangle - \frac{1}{2} \right) \cdot \left(\frac{3}{2} \langle \cos^2 \gamma \rangle - \frac{1}{2} \right) \\ &\quad \times \left(\frac{3}{2} \langle \cos^2 \Theta \rangle - \frac{1}{2} \right) \\ &= S_{\delta} \cdot S_{\gamma} \cdot S_{\Theta} \end{aligned} \quad [38]$$

The angles δ, γ and Θ may be distinct or fluctuating (partly or all), describing a microcrystalline ultrastructure

(MCU) and a liquid crystalline ultra-structure (LCU), respectively. S_y is referred to as the molecular order parameter S_{mol} .

Applying eqn [38] to the DPPA monolayer under discussion, one obtains: $S_\delta = 1$, $S_\gamma = 1$, $S_\Theta = -\frac{1}{2}$, meaning no tilt ($\delta = 0$), molecular axis (hydrocarbon chain) normal to the interface ($\gamma = 0$), and transition dipole moment normal to the molecular axis ($\Theta = 90$).

Surface Concentration and Area per Molecule

The surface concentration may be calculated using eqn [36]. The following additional information is required: (1) the integrated molar absorption coefficient related to a linear baseline from 2828 to 2871 cm^{-1} (see [Figure 9](#)) was $\int \epsilon d\tilde{\nu} = 5.7 \times 10^5 \text{ cm mol}^{-1}$, (2) the real thickness of the layer was assumed to be $d = 2.5 \text{ nm}$, (3) the number of equal functional groups $\nu = 28$ and (4) the effective thicknesses d_e for parallel- or perpendicular- polarized incident light, which were calculated from eqns [27] and [35], resulted in $d_{e,\parallel} = 3.97 \text{ nm}$ and $d_{e,\perp} = 4.30 \text{ nm}$. The mean surface concentration was found to be $3.93 \times 10^{-10} \text{ mol cm}^{-2}$, corresponding to a molecular cross-section of 0.427 nm^2 per molecule (42.3 \AA^2 per molecule). This value leads to the conclusion that the two hydrocarbon chains of a DPPA molecule predominantly determine the area per molecule, since the cross-section of an elongated hydrocarbon chain is $20\text{--}21 \text{ \AA}^2$.

Conclusions

Quantitative analysis, including orientation measurements, has been shown to be straightforward when the formalism based on Harrick's weak absorber approximation is applied. For thin adsorbed layers, such as the DPPA monolayer under discussion, the results are fairly good. Application to bulk materials may introduce systematic errors as discussed in the preceding text. If the weak absorber approximation is still to be applied, one should take care to work with an angle of incidence which is at least 15° larger than the critical angle, to avoid significant band distortions. In many cases it is possible to use quantitative data from transmission experiments to check the validity of the formalism applied to ATR data.

A general critical aspect concerning the baseline selection should be mentioned. A linear tangential baseline has been used for quantitative analysis of the symmetric CH_2 stretching vibration of DPPA (see [Figure 9](#)). Obviously the correct baseline is lower, that is the integrated absorbances used for analysis are systematically too small. The reason for this procedure is only to permit good reproducibility. While the determination of the dichroic ratio is indifferent with respect to the choice of the baseline, it is mandatory to use integrated or peak molar absorption coefficients which have been determined under

the same conditions. Even then deviations in the range of several per cent may occur among different operators.

Finally, it should be noted that ATR spectroscopy allows very good background compensation, when adequate equipment is used.

Sensitivity of ME ATR Spectroscopy

An impression of the sensitivity of stationary measurements was given the last but one section. A limit of 0.2 mAU is suggested. This limit is beaten by one order or magnitude when the ME technique is applied. As mentioned earlier, the sample must fulfil the condition of a reversible stimulation by a periodically altered external thermodynamic parameter. Here, the excellent sensitivity and instrumental stability will be demonstrated, for example, with a chemical modulation experiment performed in liquid water, a very strong absorber in the 3400 and 1640 cm^{-1} region.

In order to study the influence of immobilized charges on a lipid model membrane, an ArAc bilayer was prepared on a germanium MIRE by means of the Langmuir-Blodgett (LB) technique. The MIRE was transferred in the hydrated state from the LB trough into a flow-through cell and kept in permanent contact with an aqueous buffer solution. Since the carboxylic acid groups of the second monolayer were facing the aqueous phase, the degree of protonation could be controlled via the environmental pH. A periodic pH modulation between pH 3 and 10 induced a periodic protonation and deprotonation of the carboxylic acid group. It should be noted that the first ArAc LB layer was attached by head to the Ge MIRE. Obviously, this binding was so special that typical absorption bands of the carboxylic acid groups were not visible in the spectrum. Therefore, one may assume that the head group signals shown in [Figure 10](#) result predominately from the outer monolayer of ArAc. The stationary spectral intensity is comparable to that of the DPPA monolayer shown in [Figure 9](#). Moreover, one should note that the experiments were performed in H_2O , where in the 1640 and 3400 cm^{-1} regions there is very low spectral energy available, favouring perturbations by incomplete background compensation.

In this context, only the sensitivity and selectivity of ME techniques will be discussed. A comprehensive presentation and analysis of polarized pH modulation spectra will be given elsewhere.

Sensitivity of ME-Spectroscopy

Taking the pH-modulated spectrum shown in [Figure 10](#) as a typical example, one may estimate the sensitivity by comparing the most intense ME spectra ($\phi_{\text{PSD}} = 60^\circ / \phi_{\text{PSD}} = 90^\circ$, the maximum is expected at $\phi_{\text{PSD}} \approx 75^\circ$, consequently, $\phi_{\text{PSD}} \approx 165^\circ$ should result intensity zero) with the lowest intensity ME spectrum at $\phi_{\text{PSD}} = 0^\circ$. To check the S/N ratio, the $\phi_{\text{PSD}} = 0^\circ$ spectrum was

expanded 25 times in the CH₂ wagging region and is plotted as a dashed inset in **Figure 10**. The ordinate scaling factor for the zoomed spectrum is 4.0×10^{-5} . Comparing it with the other ME spectra (scaling factor 1.0×10^{-3}) one can conclude that bands as weak as 1.0×10^{-5} AU are still detectable.

Selectivity of pH ME

The highest selectivity of ME spectroscopy is achieved if the stimulation frequency ω and the kinetics of the stimulated process are matched, that is if $0.1 < \omega\tau_i < 10$, where τ_i denotes the i th relaxation time of the system. τ_i is a function of the rate constants involved in the stimulated process. Under these conditions, significant ω -dependent phase shifts are expected, resulting in $\phi_i = \arctan(-\omega\tau_i)$ for a linear system. Consequently, a molecular or conformational population represented by the relaxation time τ_i exhibits maximum absorbance in the ME spectrum at a PSD phase setting $\phi_i = \phi_{\text{PSD}}$, thus allowing selective detection and kinetic analysis by means of phase-resolved ME spectra. Moreover, ω acts as an additional experimental degree of freedom in this context, since information on selectivity and kinetics can be spread in the ω/ϕ_{PSD} plane which is more selective

than the unidirectional information resulting from conventional relaxation measurements.

In the actual case of pH modulation exerted on a monolayer of ArAc, there is no phase resolution observed, owing to the long modulation period of $\tau_m = 16$ min, that is no kinetic information is available. However, unambiguous discrimination between the protonated and deprotonated populations is possible. Only one characteristic example will be given here. The most prominent band from the protonated state is the C=O stretching vibration $\nu(\text{COOH})$ of the carboxylic acid group near 1700 cm^{-1} . All other bands in the ME spectrum that have the same phase belong to the protonated population, whereas the remaining bands featuring opposite sign are members of the deprotonated population. Consequently, if no phase resolution is achieved, ME spectra reduce to difference spectra, which, however, have a considerably better background and instability compensation than conventional difference spectra, since corresponding sample and reference spectra are measured and evaluated/accumulated within each period of stimulation.

Consider now the wagging region $\gamma_w(\text{CH}_2)$ of the spectra shown in **Figure 10**. The wagging motion $\gamma_w(\text{CH}_2)$ is described as in-phase displacement of both H atoms through the H-C-H plane of a methylene group, where the

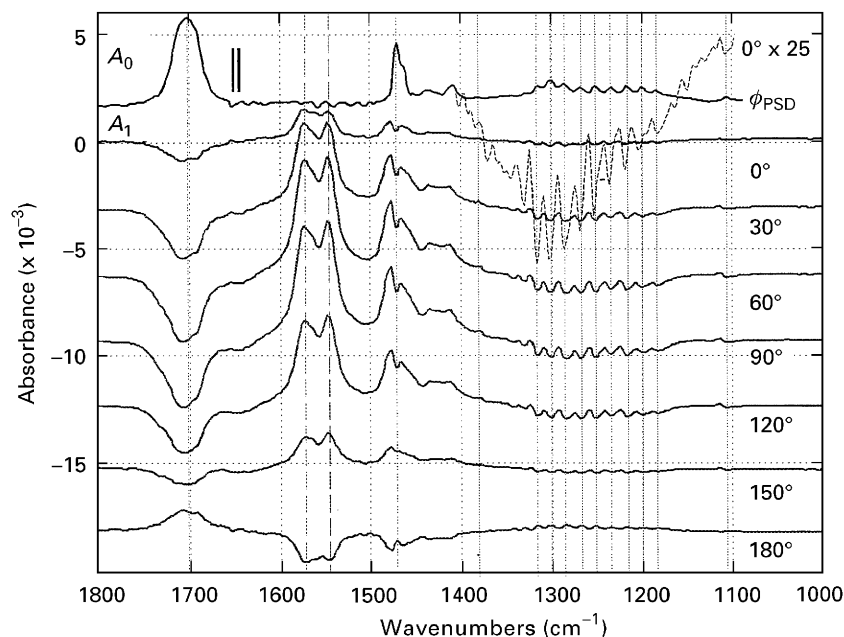


Figure 10 pH-modulated excitation (ME) of an arachidic acid (ArAc) bilayer attached to a germanium multiple internal reflection element (MIRE). ME was performed by pumping alternatively two buffer solutions (100 mM NaCl, pH 3 and 100 mM NaCl, pH 10) through the ATR cuvette with a modulation period of $\tau = 16$ min. $T = 10$ °C. Upper trace A_0 ; stationary spectrum of a protonated ArAc layer for comparison with modulation spectra. Traces A_1 ; modulation spectra at PSD phase settings $\phi_{\text{PSD}} = 0, 30, \dots, 180^\circ$. The 180° spectrum corresponds to the 0° spectrum with opposite sign, because the PSD output is proportional to $\cos(\phi - \phi_{\text{PSD}})$, see also **Figure 8**. ϕ denotes the phase difference between a given band and the stimulation. Owing to the long period of $\tau_m = 16$ min, the observed bands in the modulation spectra exhibit only two resolved ϕ values, which are 180° apart, as a consequence of the fact that the chemical relaxation time of protonation/deprotonation of ArAc is much shorter than the stimulation period. To demonstrate the excellent S/N ratio, the ordinate of the weakest modulation spectrum has been expanded in the CH₂ wagging region by a factor of 25, that is the ordinate scaling factor for the dashed spectrum results in 4.0×10^{-5} (see text).

C atom remains predominately in place. In an all-*trans* hydrocarbon chain the transition dipole moment of $\gamma_w(\text{CH}_2)$ is expected to be parallel to the chain direction. Deviations may occur, however, from coupling with a polar end group. In the stationary absorbance spectrum A_0 , one can observe nine weak bands between approximately 1180 and 1320 cm^{-1} . This sequence results from concerted wagging vibrations of all methylene groups in a hydrocarbon chain with an all-*trans* conformation. According to IR selection rules one has to expect $n/2$ IR-active vibrations for an even number n of CH_2 groups in an all-*trans* conformation. ArAc has 18 CH_2 groups per chain, resulting in the above-mentioned sequence of nine bands in accordance with theory. Since these bands are found to be in phase with $\nu(\text{COOH})$, one can conclude that deprotonation of COOH is paralleled by reversible disordering of the chain structure, most probably by introducing *gauche* defects.

Finally, it should be mentioned that $\gamma_w(\text{CH}_2)$ belongs to the group of weak absorption bands. One can conclude, therefore, that ME IR ATR spectroscopy allows significant quantitative studies on a molecular level with submonolayer quantities of weak absorbers.

Manufacturers of Reflection Accessories

Standard Equipment for Reflection Spectroscopy

ASI Sense IR Technologies, 15 Great Pasture Road, Danbury, CT 06810, USA.

Bruker Optics, Wikingenstrasse 13, D-76189 Karlsruhe, Germany.

Graseby Specac Inc., 301 Commerce Drive, Fairfield, CT 06432, USA.

Harrick Scientific Corporation, 88 Broadway, Ossining, NY 10562, USA.

International Crystal Laboratories, 11 Erie Street, Garfield, NJ 07026, USA.

Spectra-Tech, Inc., Warrington WA3 7BH, UK.

Special Equipment for SBSR-ATR and ME-ATR Spectroscopy

Optispec, Rigistrasse 5, CH-8173 Neerach, Switzerland.

See also: Electromagnetic Radiation, Industrial Applications of IR and Raman Spectroscopy, Polymer Applications of IR and Raman Spectroscopy, Surface Studies by IR Spectroscopy.

Further Reading

Baurecht D and Fringeli UP (2000) Surface charge induced conformational changes in an arachidic acid Langmuir-Blodgett bilayer observed by pH-modulated excitation FTIR ATR spectroscopy. *Langmuir* (in preparation).

- Beccard B Hapanowicz R (1995) Polarization Modulation FT-IR Spectroscopy. *Nicolet Application Note AN-9592*. Madison, WI: Nicolet.
- Blaudez D, Turllet J-M, Dufourcq D, Bard D, Buffeteau T, and Desbat B (1996) Investigation at the air-water interface using polarization modulation IR spectroscopy. *Journal of the Chemical Society, Faraday Transactions* 92: 525–530.
- Born M and Wolf E (1983) *Principles of Optics*, Chapter I. Oxford: Pergamon Press.
- Fringeli UP (1992) *In situ* infrared attenuated total reflection membrane spectroscopy. In: Mirabella FM (ed.) *Internal Reflection Spectroscopy, Theory and Applications*, Ch. 10, pp. 255–324. New York: Marcel Dekker.
- Fringeli UP (1997) Simultaneous phase-sensitive digital detection process for time-resolved, quasi-simultaneously captured data arrays of a periodically stimulated system. *PCT International Patent Application*, WO97/08598.
- Fringeli UP, Goette J, Reiter G, Siam M, and Baurecht D (1998) Structural investigation of oriented membrane assemblies by FTIR-ATR spectroscopy. In: deHaseth JA (ed.) *Fourier Transform Spectroscopy*, 11th International Conference, AIP Conference Proceedings 430, pp. 729–747. Woodbury, New York: American Institute of Physics.
- Galant J, Desbat B, Vaknin D, and Salesse Ch (1998) Polarization-modulated infrared spectroscopy and X-ray reflectivity of photosystem II core complex at the gas-water interface. *Biophysical Journal* 75: 2888–2899.
- Greenler RG (1966) Infrared study of adsorbed molecules on metal surfaces by reflection techniques. *Journal of Chemical Physics* 44: 310–315.
- Hansen WH (1973) Internal reflection spectroscopy in electrochemistry. In: Delahay P and Tobias ChW (eds.) *Advances in Electrochemistry and Electrochemical Engineering*, vol. 9, Muller RH (ed.) *Optical Techniques in Electrochemistry*, pp. 1–60. New York: Wiley.
- Hapke B (1993) *Theory of Reflectance and Emission Spectroscopy*. New York: Cambridge University Press.
- Harrick NJ (1967) *Internal Reflection Spectroscopy*. New York: Interscience; 2nd edn. (1979) Ossining, NY: Harrick, Scientific.
- Hoffmann FM (1983) Infrared reflection-absorption spectroscopy of adsorbed molecules. *Surface Science Reports* 3: 107–192.
- Kortüm G (1969) *Reflectance Spectroscopy*. New York: Springer.
- Mendelsohn R, Brauner JW, and Gericke A (1995) External infrared reflection absorption spectroscopy of monolayer films at the air-water interface. *Annual Review of Physical Chemistry* 46: 305–334.
- Mirabella FM (ed.) (1992) *Internal Reflection Spectroscopy, Theory and Application*. New York: Marcel Dekker.
- Müller M, Buchet R, and Fringeli UP (1996) 2D-FTIR ATR spectroscopy of thermo-induced periodic secondary structural changes of poly-(L)-lysine: A cross-correlation analysis of phase-resolved temperature modulation spectra. *Journal of Physical Chemistry* 100: 10810–10825.
- Picard F, Buffeteau T, Desbat B, Auger M, and Pézolet M (1999) Quantitative orientation measurements in thin films by attenuated total reflection spectroscopy. *Biophysical Journal* 76: 539–551.
- Seelig J and Seelig A (1980) Lipid conformation in model membranes and biological membranes. *Quarterly Review of Biophysics* 13: 19–61.
- Tamm L and Tatulian S (1997) Infrared spectroscopy of proteins and peptides in lipid bilayers. *Quarterly Review of Biophysics* 30: 365–429.
- Urban MW (1996) *Attenuated Total Reflectance Spectroscopy of Polymers*. Washington, DC: American Chemical Society.
- Wendlandt WWM and Hecht HG (1996) *Reflectance Spectroscopy*. New York: Interscience.
- Wenzl P, Fringeli M, Goette J, and Fringeli UP (1994) Supported phospholipid bilayers prepared by the “LB/Vesicle Method”: A Fourier transform infrared attenuated total reflection spectroscopic study on structure and stability. *Langmuir* 10: 4253–4264.
- Wooten F (1972) *Optical Properties of Solids*. New York: Academic Press.
- Zachman G (1995) A rapid and dependable identification system for black polymeric materials. *Journal of Molecular Structure* 348: 453–456.
- Zbinden R (1964) *Infrared Spectroscopy of High Polymers*. New York: Academic Press.